# Mapping oscillating magnetic fields around rechargeable batteries

Stefan Benders<sup>a</sup>, Mohaddese Mohammadi<sup>a</sup>, Matthew J. Ganter<sup>b</sup>, Christopher A. Klug<sup>c,a</sup>, Alexej Jerschow<sup>a,\*</sup>

<sup>a</sup>Department of Chemistry, New York University, New York, United States <sup>b</sup>Battery Prototyping Center, Rochester Institute of Technology <sup>c</sup>United States Naval Research Laboratory, District of Columbia, United States

#### Abstract

Power storage devices such as batteries are a crucial part of modern technology. The development and use of batteries has accelerated in the past decades, yet there are only a few techniques that allow gathering vital information from battery cells in a nonivasive fashion. A widely used technique to investigate batteries is electrical impedance spectroscopy (EIS), which provides information on how the impedance of a cell changes as a function of the frequency of applied alternating currents. Building on recent developments of inside-out MRI (ioMRI), a technique is presented here which produces spatially-resolved maps of the oscillating magnetic fields originating from the alternating electrical currents distributed within a cell. The technique works by using an MRI pulse sequence synchronized with a gated alternating current applied to the cell terminals. The approach is benchmarked with a current-carrying wire coil, and demonstrated with commercial and prototype lithium-ion cells. Marked changes in the fields are observed for different cell types.

Keywords: Current imaging, Alternating current, Oscillating field, Triggered acquisition, Rechargeable batteries

 $<sup>^*</sup>$ Corresponding author

#### Introduction

28

Power storage devices form the basis for portable electronics technology as well as for the development of electric transportation options. The demand for rechargeable batteries will significantly increase in the coming years, yet technology for adequate assessment of commercial-type cells is currently relatively limited. In particular, it is vital to establish detailed noninvasive diagnostics techniques that would allow identifying defects, predicting lifetimes, and determining critical failure mode progressions.

A commonly used technique to investigate batteries is electrical impedance spectroscopy (EIS) [1]. EIS is based on applying alternating current (AC), and recording the complex impedance as a function of current frequency [2]. EIS is further widely used to characterize materials as well as biological tissues based on the frequency response of their electrical conductivity and permittivity [3, 4, 5]. When used with batteries, EIS is often employed to assess information about internal impedance as a function of temperature, depth of discharge, and at different points in the cycling process [6, 7, 8]. Changes in the frequency response of the internal impedance of an electrochemical energy storage device provide insights into cell performance, including, for example, measures of the uniformity of the material distribution, of the quality of solid electrolyte interphase (SEI), of the electrode porosity, and of adsorption kinetics [9, 10, 11]. A major limitation of EIS is that it records only the global values for the device, and no spatial resolution is provided. While there exist techniques such as Localized Electrochemical Impedance Spectroscopy [12] or scanning electrochemical microscopy (AC-SECM)[13], these methods require access to the electrode surface and direct electrical contact, which is problematic for realistic or commercial-type cells and many other devices.

While conventional MRI is not able to investigate the processes within commercial batteries due to the difficulty for radiofrequency (RF) to penetrate through their metal casings or through the electrode layers, the inside-out MRI (ioMRI) approach is able to reveal important information by analyzing the magnetic susceptibility changes of the cell's materials via the measurement of the magnetic field distributions around the cell. This approach has been employed to detect susceptibility variations caused by changes in the cell as well as to investigate changes in direct current distributions across the device [14, 15, 16, 17, 18].

In addition, other indirect parameters such as the spatial distribution of

the magnetic field generated outside the battery caused by the current can be used as a measure of internal battery properties.

40

42

45

67

A number of MRI methods have been developed to detect electric currents via measurements of the corresponding magnetic fields using synchronized pulse sequence elements [19, 20, 21, 22, 23, 24, 25]. An approach based on a tuned spin-lock field exploits the coherent interaction between the spin-lock pulse and a fluctuating magnetic field produced by electrical currents [19]. While this approach is potentially quite powerful, there are a number of practical difficulties which limit its successful implementation for our intended application. In particular, this approach exhibits problems at low frequencies due to RF imperfections and  $T_{1\rho}$  relaxation. Other techniques comprise current density imaging (CDI) sequences[21, 22, 23] and steady state free precession (SSFP) approaches[20], both based on exploiting phase changes in the magnetic resonance signals caused by current-generated local magnetic magnetic fields. However, both approaches require precise synchronization of pulse sequence elements with the AC frequency.

Yang et al. showed, that a gradient echo sequence with a sufficient Field-of-View exhibits ghost images at regular distances which depend on the AC frequency of the current passing through a wire at a specific orientation [25]. The Fourier transform of the signal revealed these images. More recently, a method based on multiple repetition times to extend the range of frequencies accessible in measurements of brain waves was proposed by Kim et al. [24]. A Fourier transform of a series of images with a fixed repetition time was employed to recover a spectrum of oscillating field frequencies. With this approach, the delay between a certain point of the AC wave and the start of the acquisition is fixed, yet unknown. In this approach, the spectral width of the encoding of the oscillating field is not known. A second experiment set acquired with a different repetition time can recover accurate frequency information without this a priori information.

Building on lessons learnt from prior work, we present here an improved technique, suitable for mapping the oscillating magnetic fields around battery cells. In, particular the use of triggers from the current source to spectrometer as well as gating the AC current allow for more control of the experiment. This sequence and method of potentially performing battery diagnostics is henceforth referred to as inside-out Triggered Alternating Current ImagiNg employing Gating (io-TRACING). In contrast to CDI-based techniques, it is possible to scan a range of frequencies with one measurement instead of having to tailor all pulse sequence element delays to a specific

frequency. Furthermore, it is possible to obtain images at very low frequencies, e.g. 0.1-1 Hz0.1-10 Hz, which is a particularly useful range for devices such as batteries. In this range, charge-transfer processes can be observed in batteries [26]. Electric devices, which are the focus here, are excited by an external stimulus, which allows the introduction of gating of the AC, enabling a more controlled experiment. In particular, this method applies a phase-synchronized portion of the AC waveform during the evolution period of the pulse sequence (Figure 1). In the pulse sequence presented here, a spin echo imaging sequence is used with the evolution period located between the  $\frac{\pi}{2}$  and the  $\pi$  pulses. The AC phase is stepped systematically in subsequent measurements, thus producing an indirect time dimension. A Fourier transform along this dimension produces a spectrum containing information about the response of the device to the applied AC voltages. The additional imaging dimensions deliver the spatial localization of these measurements. Results acquired with a range of AC frequencies for a single loop of a wire, a commercial cell and a prototype cell are presented. The comparison between different cells demonstrates that characteristic changes can be observed in such measurements.

## 4 Pulse sequence design and theoretical background

95

90

101

103

104

105

106

107

108

110

111

This work employs a spin-echo imaging sequence (Multi-Slice-Multi-Echo, Bruker ParaVision) with modifications to allow for encoding of oscillating magnetic fields. The most significant modification is the insertion of a gate pulse in the interval between the  $\frac{\pi}{2}$  and  $\pi$  degree pulses which controls the AC current (Figure 1c). Different portions of the AC wave are sampled in this interval in a systematic way, which is defined by its starting point  $t_n$  relative to a well-defined point in the AC wave. Experimentally, this is achieved by employing a synchronized square wave triggering the spectrometer to guarantee a start at the same position in the waveform in consecutive cycles. The total encoding time  $\tau$  is held fixed, but the starting time is shifted by a multiple of the sampling delay  $\Delta \tau_{AC}$  in separate experiments (Figure 1a,c). This means that the first segment will be sampled with the interval  $[0, \tau]$ , while the next segment is sampled with  $[\Delta \tau_{AC}, \Delta \tau_{AC} + \tau]$ , etc; 16 or 32 of such measurements are typically taken to provide sufficient discrimination between different AC frequencies. The sequence of these experiments allows recording the indirect time dimension along which the AC frequency is encoded.

The AC signal is encoded in the magnetization evolution as follows. After

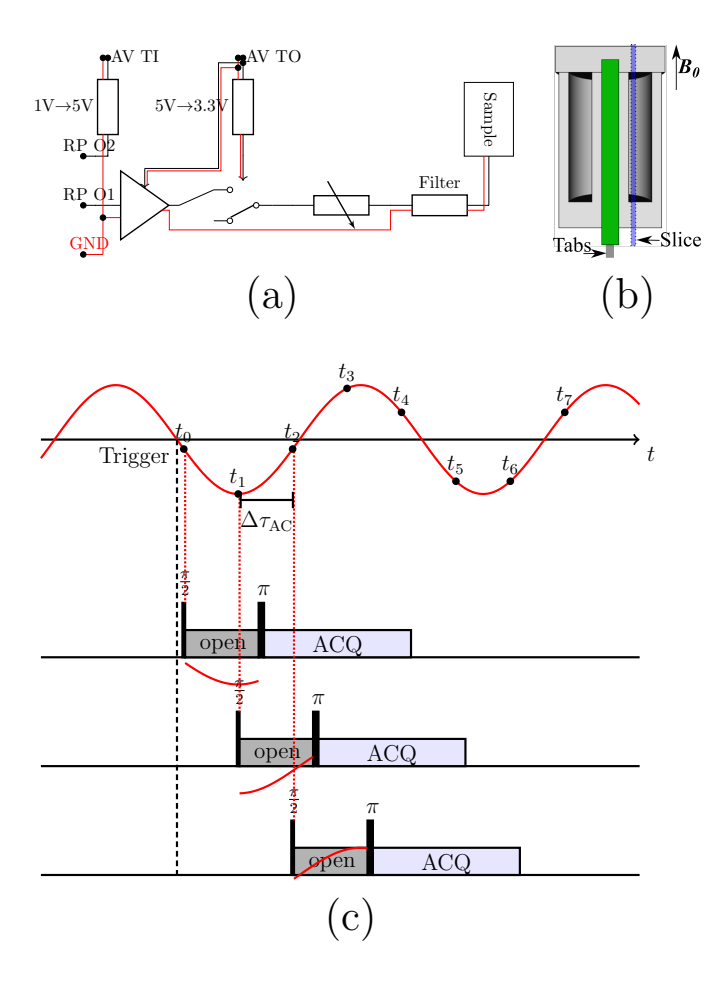


Figure 1: (a) Setup with all electronic components. See Setup and Experimental section for details. (b) 3D-printed holder for the inside-out MRI approach. The battery or coil (green) is located in the middle of the cylindrical holder with two doped water compartments located on each side of the cell/coil. The leads are soldered to the tabs/coil from the bottom of the cell and then guided down the magnet. The imaging slice is marked by the blue line. (c) Pulse sequence. A standard spin echo imaging sequence (Multi-slice-multi-echo) was employed. The sequence was modified to allow for sampling through different delay times after the trigger as well as switching the current on and off after/prior to the pulses. In each encoding segment between the pulses, a different phase is encoded, depending on the starting point  $t_n$  (depicted exemplary for point 3), which depends on  $\Delta \tau_{\rm AC}$  with  $t_n = t_0 + n \cdot \Delta \tau_{\rm AC}$ .

the excitation pulse to rotate the magnetization into the transverse plane, the magnetization evolves under the influence of the local magnetic field (Figure 1c). The field at a given position  $\mathbf{r}$  in space is composed of a static part and a superimposed oscillating field  $B_{z,\text{osc}}$ . In a frame rotating at the Larmor frequency of the static field ( $\omega_0/2\pi$ ) the signal evolution can be described by

$$S(\mathbf{r}, t_n) = M_0(\mathbf{r}) \cdot \exp\left\{-i\gamma B_{z, \text{osc.}}(\mathbf{r}) \cdot \int_{t_n}^{t_n + \tau} \sin(\omega_{\text{AC}} \cdot t') dt'\right\}. \tag{1}$$

 $S(\mathbf{r}, t_n)$  is the signal encoded by an oscillating field in the interval  $[t_n t_n + \tau]$  at a position  $\mathbf{r}$ .  $M_0$  is the bulk magnetization before applying the oscillating field,  $\gamma$  is the gyromagnetic ratio and  $B_{z,\text{osc}}(\mathbf{r})$  and  $\omega_{AC}$  are respectively the magnitude and frequency of the oscillating magnetic field. The time  $t_n$  indicates the starting point of the AC wave at the beginning of the evolution period and increments with  $\Delta \tau_{AC}$  at each step (as illustrated by the numbered points (0, 1, 2, 3,...) in Figure 1). One can therefore write  $t_n = t_0 + n \cdot \Delta \tau_{AC}$ , with  $t_0$  being the delay between trigger and AC gating (approximately 6 ms in the experiments done here, the exact delay is not important as long as it is constant).

120

122

126

128

130

132

To simplify discussions, the location-dependence in Equation (1) and associated symbols will be omitted, with the understanding that location-resolved signals will be provided via the imaging portion of the pulse sequence.

The integral can be solved and replaced by an infinite sum of cosine terms via the Jacobi-Anger expansion,

$$S(t_n) = \left(J_0\left(\frac{\gamma B_{z,\text{osc.}}}{\omega_{\text{AC}}}\right) + \sum_{k=1}^{\infty} 2i^k J_k\left(\frac{\gamma B_{z,\text{osc.}}}{\omega_{\text{AC}}}\right) \cos\left(k \cdot \omega_{\text{AC}} \cdot t_n + k \cdot \omega_{\text{AC}} \cdot \tau\right)\right)$$
$$\cdot \left(J_0\left(-\frac{\gamma B_{z,\text{osc.}}}{\omega_{\text{AC}}}\right) + \sum_{l=1}^{\infty} 2i^l J_l\left(-\frac{\gamma B_{z,\text{osc.}}}{\omega_{\text{AC}}}\right) \cos\left(l \cdot \omega_{\text{AC}} \cdot t_n\right)\right)$$
(2)

As can be seen, a series of oscillating terms at multiples of the base frequency arise. Further details of the derivation are provided in the Appendix. While the series expansion provides conceptual insights, a numerical calculation of Eq. (1) and its Fourier transform was found more practical, and was performed using MatLab (MathWorks, Natick, MA). These simulations obtained for a single frequency and fixed  $\tau$  show the expected behaviour of peaks

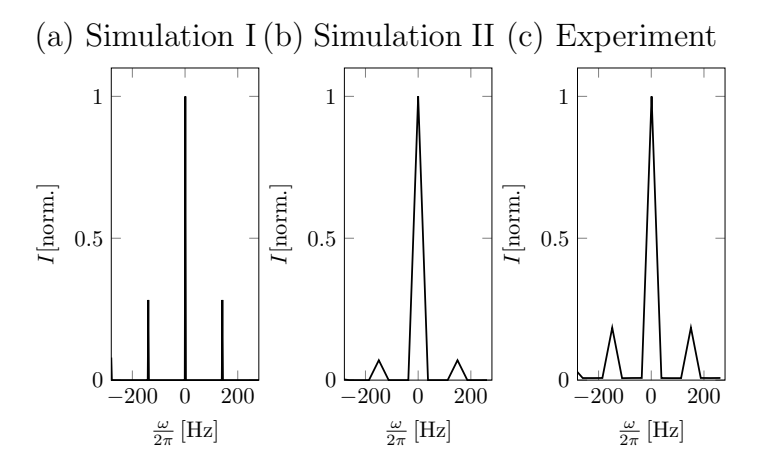


Figure 2: (a): Simulation of the io-TRACING spectrum at 140 Hz AC frequency and  $3.21\,\mathrm{ms}~\tau$  with 1024 points of AC sampling and a  $\Delta\tau_{\mathrm{AC}}$  of 1.786 ms. (b) The same simulation with 16 points (c) Result from an experiment with 16 points of AC sampling. The summed absolute values for each frequency over all pixels in a 2D slice are shown for an experiment with  $\omega_{\mathrm{AC}}/2\pi=140\,\mathrm{Hz}$  AC frequency and 54 mA AC current.

at multiples of the AC frequency and zero as seen in Figure 2a. Plotting the ratio of the respective frequency peak to the zero-frequency peak versus AC frequency reveals a magnitude sinc-shaped behaviour, i.e. a general decay with AC frequency as well as a substructure leading to zero intensity nodes at multiples of  $\frac{1}{\tau}$  (Figure S1). A choice of a small  $\tau$  changes the position of these nodes, but reduces the encoding strength.

The strong dependence on  $\frac{\omega_{\rm AC}}{2\pi}$ , with the envelope in Figure S1 decaying with a multiple of  $\frac{1}{\frac{\omega_{\rm AC}}{2\pi}}$ , also suggests that this method allows the measurement of frequencies of up to approximately 1-2 kHz.

The spectral width for AC-frequency encoding is given by  $SW_{AC} = \frac{1}{\Delta \tau_{AC}}$  (Figure 1). As a consequence, this method can be employed to scan for an unknown frequency by employing a small sampling delay and many steps. The acquisition can be tailored to a specific frequency range by adjusting the sampling delay according to this expression. A compromise can often be found between sufficient spectral resolution and experiment duration. This approach is particularly important at low frequencies. For example, for 0.1 Hz, the sampling delay,  $\Delta \tau_{AC}$ , becomes 2.5 s for a io-TRACING spectral width of 0.4 Hz, and the experiment times for 8, 16 or 32 points in the indirect AC dimension (phase dimension 64 points, 4 scans, TR 125 ms) become roughly

6.4 h, 24.2 h and 93.9 h, respectively. The inconvenient lengthening of experiment times at very small frequencies is also known in EIS.

The spectral resolution is given by the spectral width for AC-frequency encoding and the number of encoded segments  $n_{\rm enc}$ :  $\frac{{\rm SW}_{AC}}{n_{\rm enc}} = \frac{1}{\Delta \tau_{\rm AC} \cdot n_{\rm enc}}$ . The sampling delay should be set to capture all frequencies in the sample, leading to the conditions  ${\rm SW}_{\rm AC} > 2\frac{\omega_{\rm AC}}{2\pi}$ , so  $\Delta \tau_{\rm AC} < \frac{\pi}{\omega_{\rm AC}}$ , and  $n_{\rm enc}$  set to distinguish between different frequencies, or the frequency and the zero peak, so  $\frac{{\rm SW}_{\rm AC}}{n_{\rm enc}} < \frac{\Delta \omega_{\rm AC}}{2\pi} \to n_{\rm enc} > \frac{2\pi {\rm SW}_{\rm AC}}{\Delta \omega_{\rm AC}} \to n_{\rm enc} > \frac{2\pi}{\Delta \omega_{\rm AC}}$ . The encoded signal (after Fourier transformation along this dimension) is proportional to the field in the low-field regime for a specific  $\tau$  (for  $\tau$ =3.21 ms and  $B < 1.5\,\mu{\rm T}$ ) (Figure S3), hence it is a direct measure of the z field strength at a certain frequency. There is a functional relationship between intensity and frequency (Figure S1) , which requires precise calibration with the encoding time  $\tau$ . While this parameter can be set, switching times of electronic components alter the value. Here, a field estimate based on simulations is pursued, which is inaccurate at frequencies close to  $\frac{1}{\tau}$ . In principle, experimental calibration is possible with e.g. a coil fixed in position and immersed in the medium.

# Setup and experimental

The experimental schematic is shown in Figure 1a. The AC waveform was generated with a Red Pitaya STEMLab 125-14 FPGA controller unit. The generated signal was amplified with a Stanford Research Systems SR560 Low Noise-Amplifier (Gain 1000). To trigger the spectrometer from the Red Pitaya control unit, a square wave was generated on the second output of the unit and then shifted from 1 V to 5 V employing an Arduino UNO. The amplifier blanking was realized with an output of the spectrometer. In the case of batteries, a switch (PE42020, Peregrine) was employed to prevent DC discharge against the output impedance of the amplifier when AC current is not applied to the battery. This switch is able to reliably disconnect the battery from the generation at the frequencies employed in this study. The output is fed to the measurement cell through a variable resistor to fine tune the current level, and a filter to remove high frequency components in the RF region.

The experiment was set up such that the magnetic fields were mapped around the battery with a suitable detection medium and MRI sequence according to the ioMRI strategy [17, 15]. A polylactic acid (PLA) cell holder (outer diameter 19.75 mm) was 3D-printed consisting of a slot to hold the

battery and two semicircular chambers next to that slot (Figure 1b). The chambers were filled with aqueous 0.1 M CuSO<sub>4</sub> solution. The coil used in the evaluation experiments consisted of a single loop with a diameter Two batteries were employed in this study. (1) A Rochester of 18 mm. Institute of Technology (RIT) cell: Pouch cell Li-ion battery with 250 mAh capacity. The battery is made of five layers of stacked-cut graphite anode and NMC cathode electrodes. The cathode is composed of Co (5.97 wt%), O (19.46 wt%), Ni (14.46 wt%, and Mn (9.19 wt%). (2) Powerstream (PS) cells: Jelly rolled lithium ions battery with 600 mAh capacity. The graphite and NMC electrodes are rolled in twelve active layers and packed inside an aluminum pouch case. Both batteries are made from graphite anode, aluminum and copper current collectors. The cathode in the PS battery is made of Co (44.76 wt%), O (33.20 wt%), Ni (4.79 wt%), Mn (2.99 wt%). Both cells were fully charged prior to the experiment. The dimensions of the RIT and PS cells are  $65.7 \times 42.5 \,\mathrm{mm^2}$ , and  $40 \times 30 \,\mathrm{mm^2}$ , respectively. Consequently, the battery tabs of the RIT cell are located further out of the measurement volume than the PS cells. Since the holder has a 10 mm bottom to prevent leaking, the lowest 10 mm of the battery close to the tabs are not represented. Furthermore, on the opposite side, the image is limited by the excitation volume of the RF coil.

195

197

198

200

201

202

203

204

206

208

210

211

212

213

214

215

216

217

219

220

221

222

224

226

227

A 400 MHz Bruker Avance magnet with a 57 mm gradient system (max. gradient strength 0.3 T/m) and a 40 mm  $^{1}{\rm H}$  coil was employed for the experiments. The battery or coil was rotated with the holder to align parallel with the  $B_{1}$  field to minimize artifacts. The main experimental parameters were set as follows: echo time 10 ms (except stated otherwise); repetition time 120 ms; number of averages 2; number of repetitions (AC frequency dimension, number of different phases sampled) 8 (PS cell < 0.25 Hz)/16 (PS cell > 0.25 Hz, coil)/32 (RIT cell); sampling delay for the AC frequency:  $\frac{1}{4\cdot\frac{\omega_{\rm AC}}{2\pi}}$  (set with the expected AC frequency, see the section on pulse sequence design and theoretical background; pulse shapes: sinc3, excitation pulse length 2 ms (90°); refocusing pulse length 1.267 ms 1.5 ms for coil experiments), field-of-view (except different orientations)  $40\times30~{\rm mm}^{2}$ ; matrix size  $128\times64/32$ ; slice thickness 2 mm; dwell time 20 µs. With these settings, the refocusing pulse matches (coil experiment) or exceeds (battery experiment) the excitation pulse bandwidth.

The number of samples in the AC dimension is NR, and the increment of the delay  $t_n$  is  $\Delta \tau_{AC}$ . For each of these, a full k-space is acquired.

For a two-dimensional image such as those obtained in this study, the data is subject to a three-dimensional Fourier transform, where two dimensions represent image dimensions and one dimension the AC field frequency dimension. Each pixel of the image is then associated with a spectrum of NR points. To identify the dominating frequencies, all pixels are integrated and the three highest peaks are identified. Then, the data point number of e.g. the positive peak is identified, its intensity set in relation to the zero-frequency peak intensity, here referred to as relative intensity  $I_{\text{ratio}} = |I_{\frac{\omega_{\text{AC}}}{2\pi}}|/|I_0|$ , which then can be plotted as an image.

## Evaluation of the technique with a single loop coil

A single-loop coil was used to test the measurement setup and to demonstrate the ability to map the oscillating magnetic fields. According to the presented theoretical considerations, the Fourier transform of the signal features peaks at zero and  $\pm n \frac{\omega_{\text{AC}}}{2\pi}$ . If the corresponding spectra of all pixels are summed up, a global spectrum at a frequency of  $\frac{\omega_{\text{AC}}}{2\pi}$  is obtained, which shows the expected behavior (Figure 2, c). Overtone signal peaks may be observed at lower intensities at multiples of the base frequency.

The spatial distribution of the magnetic field does not change with frequency for the single loop measurements. This is expected as the coil impedance does not change in the frequency range of the applied current (0.1-4000 Hz). In the images of a slice parallel to the coil plane, the z-component of the field can be observed with a zero node in the middle of the coil and two regions of high intensity (Figure 3). A plane parallel to the coil at a certain distance is expected to show a z-field, which increases from the center position upwards and then decreases beyond the coil radius (see the simulations in Figure S3). The sign of the field was not determined with this approach due to magnitude processing. The phase of single pixels is frequency dependent, as the Fourier terms in the supporting information reveal, but the dependence is complex. In the future, it may be possible to obtain phase information of the field by employing a phase-sensitive acquisition scheme.

While the pattern of the observed field magnitude remains largely the same as a function of frequency, the overall intensity changes, as expected from numerical simulations of Equation 1 (Figure S1). Furthermore, the encoding strength can be controlled by a change of the echo time, or more precisely the encoding time  $\tau$  (Figure S4). In the bottom row of Figure 3, the intensity variation with frequency can be observed. To compare field

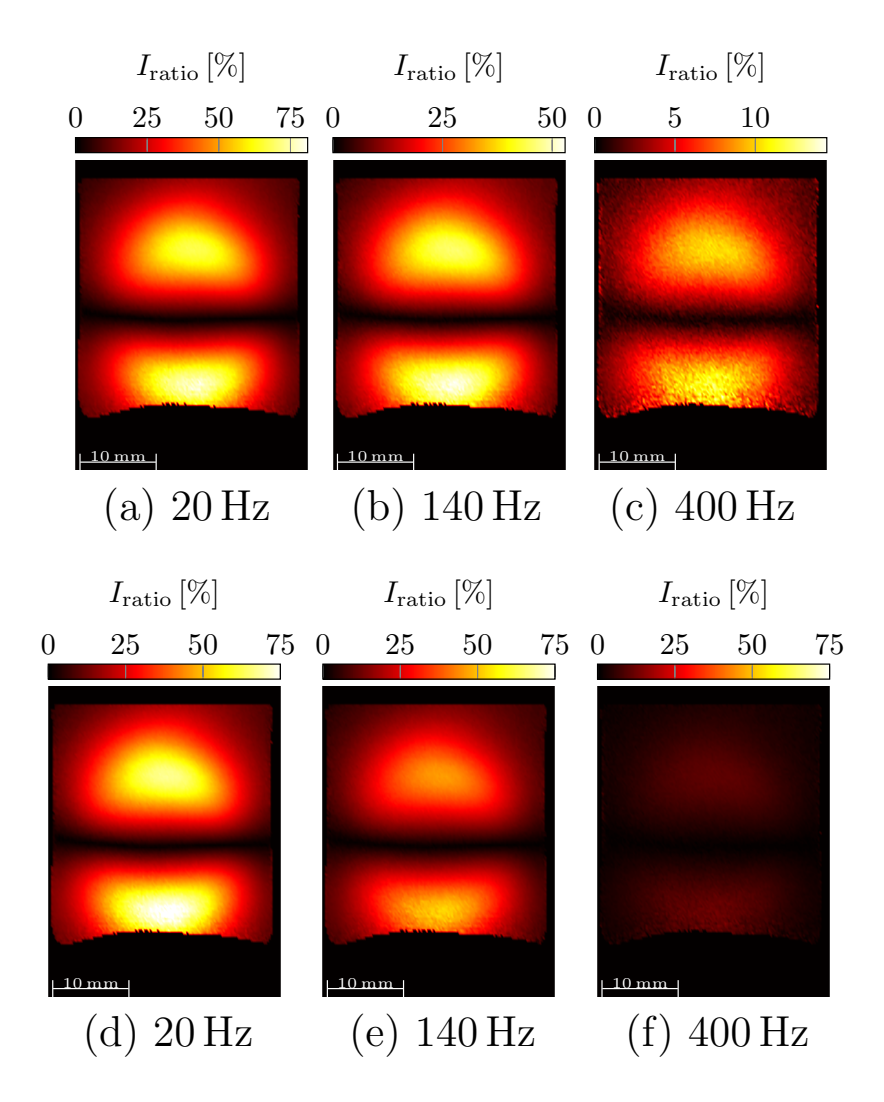


Figure 3: Comparison of the positive frequency part of the spectrum at different AC frequencies with a current of 54 mA. While the absolute intensity changes (bottom row), the relative patterns remain (top row). 16 experiments with different parts of the waveform have been employed for reconstruction resulting in  $t_n$  of 0 to 15  $\Delta \tau_{\rm AC}$ .

pattern changes, it is desirable to have a common scale. Therefore, the images have to be multiplied by a factor related to the physical field, which can be estimated from simulations. The integrated signal ratio between the first frequency peak at  $\omega = \omega_{AC}$  and the  $\omega = 0$  peak over the whole image at these frequencies should therefore follow the simulated response. In Figure 4, the experimental data agree relatively well with the simulation, although the encoding time seems to be slightly different due to electronic part switching times, causing shifts in the pattern. Although the switching times for the amplifier blanking are given by 5 µs and 15 µs, respectively, the best match was found by adding a 60 µs delay to the simulation. Furthermore, the intensity of the 20 ms echo time curves do not seem to line up. At such a high echo, the encoding of field information is strong, which causes inverted ratios of  $\omega = 0$  and  $\omega = \omega_{AC}$  peaks and therefore elevated errors. This is enhanced by the normalization of the intensity in this Figure in order to compare between simulation and experiment. Smaller encoding/echo times lead to lower intensity as also shown in Figure S1. Furthermore, as expected, the intensity is a function of current and scales proportionally (Figure S5).

268

270

271

273

274

275

276

277

270

281

282

283

284

285

286

287

288

289

290

291

292

293

294

296

298

300

The numerical simulations can also serve as a way to estimate the field. The ratio of peaks, which has a magnitude sinc-like behaviour with AC frequency as shown in Figures 4 and S1, can be employed to calculate a factor to transform the data into field estimates. However, due to small differences in encoding time caused by electronic component switching, the curves of experiment and simulation do not completely agree with each other and seem to be shifted (see above). Therefore, especially at frequencies close to the zero-intensity nodes, this method is not very accurate. The peak field amplitude is estimated to be 1.5 μT. At half of the current, the intensity is also approximately halved leading to a field estimate of 0.75µT (Figure S5). A simulation with in-house Matlab code shows the same field pattern and reproduces the observed field values up to a residual discrepancy at a level of 0.93 µT (Figure S3), 7.5 mm slice position). Small differences in sample positioning can lead to strong changes in magnitude with the current sample arrangement. Therefore, a small offset of the distance leads to a slightly larger or smaller value. Evidence for this assumption can be found in Figure S6 (b), where both sides show different intensities. While agreement between experiment and simulation is good, more precise positioning will allow better quantification of overall amplitudes and field distributions. In addition, inaccuracies in the field estimate can arise due to division by small values near the nodes in Figure 4.

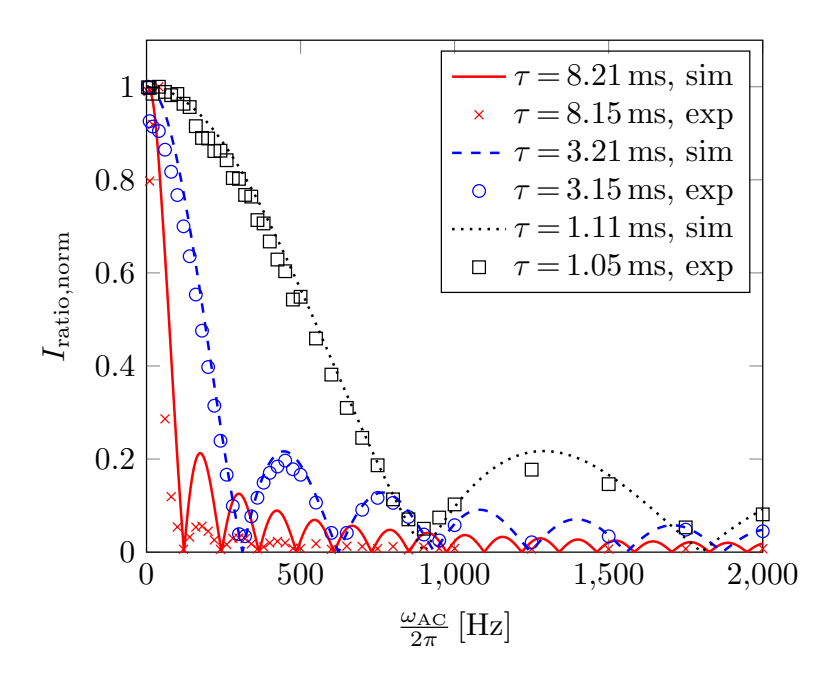


Figure 4: Comparison of experimental (positive frequency, single loop,  $54\,\mathrm{mA}$ , slice distance from coil approx.  $7.5\,\mathrm{mm}$ ) and simulated data. The experimental data represent an integral of the whole image and all curves have been normalized for comparison purposes. The encoding time for the AC frequency,  $\tau$  is related to the echo time (TE) via  $\tau = \frac{\mathrm{TE}}{2} - 1.85\,\mathrm{ms}$ , since the AC field is turned on only during the first echo period, and TE also includes additional pulse durations. 16 experiments with different parts of the waveform have been employed for reconstruction of each point. A delay of 60µs has been added to the simulation data to account for imperfections in AC feed current amplifier switching in the experiment. With these adjustments a near-perfect agreement can be obtained, especially at the shorter times. Even the uncorrected curves show very good agreement (see Figure S7)

# Application of the technique to commercial batteries

The battery tabs are located at the top of the images shown in Figure 5. Measurements of a PS jelly-rolled 600 mAh cell show small changes with frequency. A zero node can be observed at all frequencies (Figure 5 (e-h)). One notable observation is that the thickness of the zero node in the images decreases slightly with frequency. Furthermore, a small change of the top pattern can be observed at low frequencies. Another change observed at very low AC frequencies (below 2 Hz) is a broadening of the io-TRACING spectrum peaks to more than one point, leading to minor intensity reductions in the corresponding images. The peak field estimate for this cell is in the range of 700750 nT.

For a RIT cell with 250 mAh capacity, there are significant changes with frequency. While at lower frequencies, the intensity is at the tabs (Figure 5 a), the pattern changes significantly with frequency (Figure 5 b-d). The field is in the range of  $300-\frac{1500830}{1500}$  nT.

These results are encouraging with respect to demonstrating the ability to detect AC fields originating from cells. The fact that marked differences between the different types of cells are seen shows that battery characteristics do leave their marks on the measurements. The two cell types differ in their designs, capacities, and form factors. Notably one has stacked electrodes, and the other rolled ones. Furthermore, the observation that the pattern changes with frequency for only one of them indicates that the AC measurement holds a lot more information than can presently be extracted.

It is recognized, however, that the present work does not constitute proof that the AC measurement provides significant improvements in the diagnostic ability or differentiation between cells. More work with a careful selection of cell types, designs, and properties, would be necessary to delineate the connection between underlying changes in electrochemical behavior and the measured oscillating fields in cells, which exceeds the scope of this article.

Future improvements of the method could include acceleration with advanced imaging schemes such as Rapid Acquisition with Relaxation Enahancement (RARE)[27], a constant-time implementation to remove the frequency dependence on the signal intensity, and a lock-in detection to extract the sign and phase of the field and improve the quantification of the field. The developed methodology could also be applied to devices other than the battery cells considered here, including, for example, fuel cells, and other electrochemical testing chambers in both inside-out and conventional imple-

41 mentations.

343

345

347

349

350

351

352

353

355

358

362

# Conclusions

A new technique is presented, allowing measuring oscillating magnetic fields around battery cells. In contrast to many other techniques requiring synchronization of the AC frequency with the whole pulse sequence, in the current io-TRACING approach, the AC sampling conditions can be set independently of the sequence. The technique relies on triggering from a frequency generator as its only input to insure a consistent start point for the sequence. The method is relatively easy to implement with minor electronic parts external to the spectrometer. In combination with the inside-out MRI (ioMRI) approach, complicated systems such as batteries and other devices can be investigated. In this work, changes between different Li-ion battery types were observed. The developed technique could be applied to other devices and processes, and may aid in nondestructive battery characterization, by providing information akin to a localized version of electrochemical impedance spectroscopy.

# Acknowledgements

This work was supported the US National Science Foundation under award CBET 1804723. Furthermore, the authors like to thank Leeor Alon for fruitful discussions. CAK acknowledges support for this research from the Office of Naval Research (ONR) through the base program NRL core funding.

### $\mathbf{A}_{\mathbf{63}}$ Appendix A.

Approximations to the Fourier transform of the signal equation

The integrated signal equation is (with  $f_{AC} = \frac{\omega_{AC}}{2\pi}$ ):

$$S(t_n) = M_0 \cdot \exp\left\{i \cdot \gamma \frac{B_{z,\text{osc.}}}{2\pi f_{\text{AC}}} \cdot \left(\cos(2\pi f_{\text{AC}} \cdot (t_n + \tau)) - \cos(2\pi f_{\text{AC}} \cdot t_n)\right)\right\}$$
(A.1)

This expression can be rewritten with the help of the Jacobi-Anger expansion

$$\exp(iz\cos\Phi) = J_0(z) + 2\cdot\sum_{n=1}^{\infty} i^n J_n(z)\cos(n\Phi), \tag{A.2}$$

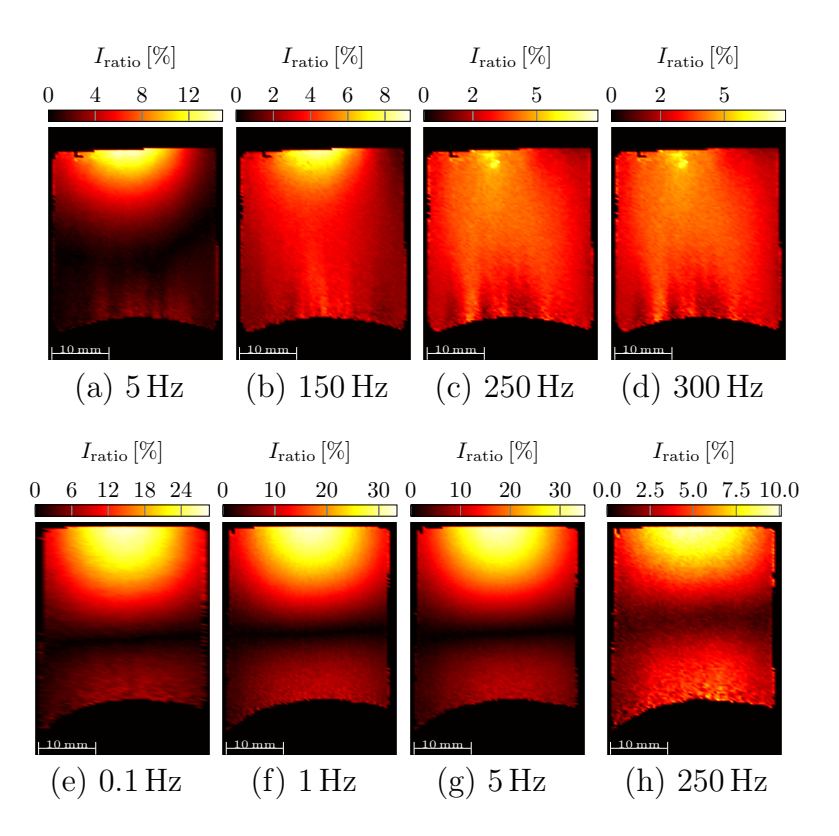


Figure 5: Relative measurements of the oscillating fields generated by 50 mA AC current in various Li-ion batteries at different driving AC frequencies. Slices are parallel to the battery at a distance of approx. 7.5 mm from the center with the battery tabs being located at the top of the image. (a)-(d) are maps from a 250 mAh RIT cell, which has a stacked electrode design. The images in (e)-(h) are from a 600 mAh PS jelly-rolled cell. 16 experiments with different parts of the waveform have been employed for reconstruction of each point of the PS images ( $t_n$  from 0 to 15  $\Delta \tau_{\rm AC}$ ), while 32 were used for the RIT cell ( $t_n$  from 0 to 31  $\Delta \tau_{\rm AC}$ ). A different scaled version can be found in Figure S8.

368 which leads to:

369

$$S(t_n) = \left(J_0\left(\frac{\gamma B_{z,\text{osc.}}}{2\pi f_{\text{AC}}}\right) + \sum_{k=1}^{\infty} 2i^k J_k\left(\frac{\gamma B_{z,\text{osc.}}}{2\pi f_{\text{AC}}}\right) \cos\left(k \cdot 2\pi f_{\text{AC}} \cdot t_n + k \cdot 2\pi f_{\text{AC}} \cdot \tau\right)\right)$$

$$\cdot \left(J_0\left(-\frac{\gamma B_{z,\text{osc.}}}{2\pi f_{\text{AC}}}\right) + \sum_{l=1}^{\infty} 2i^l J_l\left(-\frac{\gamma B_{z,\text{osc.}}}{2\pi f_{\text{AC}}}\right) \cos\left(l \cdot 2\pi f_{\text{AC}} \cdot t_n\right)\right)$$
(A.3)

The Jacobi-Anger expansion consists of a series of Bessel functions. Replacing the cosine functions with sums of exponentials using the Euler formula allows formally writing down the Fourier transformation of this expression. As an example, solutions are provided considering cutoffs of  $n \leq 5$  and  $m \leq 5$ . These expressions are provided for the zero-frequency peak I(0), and the  $\pm f_{AC}$  frequency peak amplitudes  $I(\pm f_{AC})$  are provided below, and a full numerical solution is plotted in Figure S1.

$$\begin{split} I(0) &= \sqrt{2\pi} \{ \\ e^{-5i\tau 2\pi f_{\rm AC}} J_0^2 \left( \frac{\gamma B_{z,\rm osc.}}{2\pi f_{\rm AC}} \right) + \left( e^{4i\tau 2\pi f_{\rm AC}} + e^{6i\tau 2\pi f_{\rm AC}} \right) J_1^2 \left( \frac{\gamma B_{z,\rm osc.}}{2\pi f_{\rm AC}} \right) \\ &+ e^{3i\tau 2\pi f_{\rm AC}} J_2^2 \left( \frac{\gamma B_{z,\rm osc.}}{2\pi f_{\rm AC}} \right) + e^{7i\tau 2\pi f_{\rm AC}} J_2^2 \left( \frac{\gamma B_{z,\rm osc.}}{2\pi f_{\rm AC}} \right) \\ &+ e^{2i\tau 2\pi f_{\rm AC}} J_3^2 \left( \frac{\gamma B_{z,\rm osc.}}{2\pi f_{\rm AC}} \right) + e^{8i\tau 2\pi f_{\rm AC}} J_3^2 \left( \frac{\gamma B_{z,\rm osc.}}{2\pi f_{\rm AC}} \right) \\ &+ e^{i\tau 2\pi f_{\rm AC}} J_4^2 \left( \frac{\gamma B_{z,\rm osc.}}{2\pi f_{\rm AC}} \right) + e^{9i\tau 2\pi f_{\rm AC}} J_4^2 \left( \frac{\gamma B_{z,\rm osc.}}{2\pi f_{\rm AC}} \right) \\ &+ e^{10i\tau 2\pi f_{\rm AC}} J_5^2 \left( \frac{\gamma B_{z,\rm osc.}}{2\pi f_{\rm AC}} \right) + J_5^2 \left( \frac{\gamma B_{z,\rm osc.}}{2\pi f_{\rm AC}} \right) \\ &\} \quad (\rm A.4) \end{split}$$

$$I(f_{AC}) = i\sqrt{2\pi}e^{-4i\tau 2\pi f_{AC}} \left\{ -1 + e^{i\tau 2\pi f_{AC}} J_0 \left( \frac{\gamma B_{z,osc.}}{2\pi f_{AC}} \right) J_1 \left( \frac{\gamma B_{z,osc.}}{2\pi f_{AC}} \right) - e^{3i\tau 2\pi f_{AC}} \left( -1 + e^{3i\tau 2\pi f_{AC}} \right) J_2 \left( \frac{\gamma B_{z,osc.}}{2\pi f_{AC}} \right) J_1 \left( \frac{\gamma B_{z,osc.}}{2\pi f_{AC}} \right) + e^{2i\tau 2\pi f_{AC}} J_2 \left( \frac{\gamma B_{z,osc.}}{2\pi f_{AC}} \right) J_3 \left( \frac{\gamma B_{z,osc.}}{2\pi f_{AC}} \right) - e^{7i\tau 2\pi f_{AC}} J_2 \left( \frac{\gamma B_{z,osc.}}{2\pi f_{AC}} \right) J_3 \left( \frac{\gamma B_{z,osc.}}{2\pi f_{AC}} \right) + e^{i\tau 2\pi f_{AC}} J_3 \left( \frac{\gamma B_{z,osc.}}{2\pi f_{AC}} \right) J_4 \left( \frac{\gamma B_{z,osc.}}{2\pi f_{AC}} \right) - e^{8i\tau 2\pi f_{AC}} J_3 \left( \frac{\gamma B_{z,osc.}}{2\pi f_{AC}} \right) J_4 \left( \frac{\gamma B_{z,osc.}}{2\pi f_{AC}} \right) - e^{9i\tau 2\pi f_{AC}} J_4 \left( \frac{\gamma B_{z,osc.}}{2\pi f_{AC}} \right) J_5 \left( \frac{\gamma B_{z,osc.}}{2\pi f_{AC}} \right) + J_4 \left( \frac{\gamma B_{z,osc.}}{2\pi f_{AC}} \right) J_5 \left( \frac{\gamma B_{z,osc.}}{2\pi f_{AC}} \right)$$

$$\left\{ (A.5) \right\}$$

$$I(-f_{AC}) = i\sqrt{2\pi}e^{-5i\tau^{2}\pi f_{AC}} \left\{ -e^{4i\tau^{2}\pi f_{AC}} \left( -1 + e^{i\tau^{2}\pi f_{AC}} \right) J_{0} \left( \frac{\gamma B_{z,\text{osc.}}}{2\pi f_{AC}} \right) J_{1} \left( \frac{\gamma B_{z,\text{osc.}}}{2\pi f_{AC}} \right) - e^{3i\tau^{2}\pi f_{AC}} \left( -1 + e^{3i\tau^{2}\pi f_{AC}} \right) J_{1} \left( \frac{\gamma B_{z,\text{osc.}}}{2\pi f_{AC}} \right) + e^{2i\tau^{2}\pi f_{AC}} J_{2} \left( \frac{\gamma B_{z,\text{osc.}}}{2\pi f_{AC}} \right) J_{3} \left( \frac{\gamma B_{z,\text{osc.}}}{2\pi f_{AC}} \right) - e^{7i\tau^{2}\pi f_{AC}} J_{2} \left( \frac{\gamma B_{z,\text{osc.}}}{2\pi f_{AC}} \right) J_{3} \left( \frac{\gamma B_{z,\text{osc.}}}{2\pi f_{AC}} \right) + e^{i\tau^{2}\pi f_{AC}} J_{3} \left( \frac{\gamma B_{z,\text{osc.}}}{2\pi f_{AC}} \right) J_{4} \left( \frac{\gamma B_{z,\text{osc.}}}{2\pi f_{AC}} \right) - e^{8i\tau^{2}\pi f_{AC}} J_{3} \left( \frac{\gamma B_{z,\text{osc.}}}{2\pi f_{AC}} \right) J_{4} \left( \frac{\gamma B_{z,\text{osc.}}}{2\pi f_{AC}} \right) - e^{9i\tau^{2}\pi f_{AC}} J_{4} \left( \frac{\gamma B_{z,\text{osc.}}}{2\pi f_{AC}} \right) J_{5} \left( \frac{\gamma B_{z,\text{osc.}}}{2\pi f_{AC}} \right) + J_{4} \left( \frac{\gamma B_{z,\text{osc.}}}{2\pi f_{AC}} \right) J_{5} \left( \frac{\gamma B_{z,\text{osc.}}}{2\pi f_{AC}} \right)$$

$$\left\{ (A.6) \right\}$$

### 76 References

<sup>377</sup> [1] M. Galeotti, L. Cinà, C. Giammanco, S. Cordiner, A. Di Carlo, <sup>378</sup> Performance analysis and SOH (state of health) evalua-<sup>379</sup> tion of lithium polymer batteries through electrochemical

- impedance spectroscopy, Energy 89 (2015) 678-686. URL:

  http://www.sciencedirect.com/science/article/pii/S0360544215007756.

  doi:10.1016/j.energy.2015.05.148.
- [2] E. Barsoukov, J. R. Macdonald, Impedance Spectroscopy: Theory, Experiment, and Applications, John Wiley & Sons, 2018. Google-Books TudRDwAAQBAJ.
- [3] J. Estrela da Silva, J. P. Marques de Sá, J. Jossinet, Classification of breast tissue by electrical impedance spectroscopy, Medical and Biological Engineering and Computing 38 (2000) 26–30. URL: https://doi.org/10.1007/BF02344684. doi:10.1007/BF02344684.
- [4] M. Glatthaar, M. Riede, N. Keegan, K. Sylvester-Hvid, B. Zim-390 mermann, M. Niggemann, A. Hinsch, A. Gombert, Effi-391 ciency limiting factors of organic bulk heterojunction solar 392 cells identified by electrical impedance spectroscopy, Solar 393 Energy Materials and Solar Cells (2007)91 390–393. URL: 394 http://www.sciencedirect.com/science/article/pii/S0927024806004235. 395 doi:10.1016/j.solmat.2006.10.020. 396
- <sup>397</sup> [5] R. J. Halter, A. Schned, J. Heaney, A. Hartov, S. Schutz, K. D. Paulsen, Electrical impedance spectroscopy of benign and malignant prostatic tissues, The Journal of Urology 179 (2008) 1580–1586. doi:10.1016/j.juro.2007.11.043.
- [6] P. Singh, R. Vinjamuri, Χ. Wang, D. Reisner, Fuzzy 401 modeling logic of EIS measurements on lithium-ion bat-402 Electrochimica Acta 51 (2006)teries. 1673 - 1679. URL: 403 http://www.sciencedirect.com/science/article/pii/S0013468605007851. 404 doi:10.1016/j.electacta.2005.02.143. 405
- 406 [7] A. Eddahech, O. Briat, E. Woirgard, J. M. Vinassa, Remaining useful life prediction of lithium batteries in calendar ageing for automotive applications, Microelectronics Reliability 52 (2012) 2438–2442. URL: http://www.sciencedirect.com/science/article/pii/S002627141200282X. doi:10.1016/j.microrel.2012.06.085.
- [8] C. Pastor-Fernández, W. Dhammika Widanage, J. Marco, M.-Á. Gama-Valdez, G. H. Chouchelamane, Identification and quantification of ageing mechanisms in Lithium-ion batteries using the EIS technique, in:

- 2016 IEEE Transportation Electrification Conference and Expo (ITEC), 2016, pp. 1–6. doi:10.1109/ITEC.2016.7520198.
- [9] P. Verma, P. Maire, P. Novák, A review of the features and analyses of the solid electrolyte interphase in Li-ion batteries, Electrochimica Acta 55 (2010) 6332-6341. URL:

  http://www.sciencedirect.com/science/article/pii/S0013468610007747.
  doi:10.1016/j.electacta.2010.05.072.
- [10] J.-B. Jorcin. Μ. Ε. Orazem. N. Pébère. В. Tribollet, 421 CPE analysis by local electrochemical impedance spec-422 Electrochimica Acta 51 (2006)1473–1479. URL: troscopy. 423 http://www.sciencedirect.com/science/article/pii/S0013468605008285. 424 doi:10.1016/j.electacta.2005.02.128. 425
- themical Impedance Spectroscopy Study of a Lithium/Sulfur Battery: Modeling and Analysis of Capacity Fading, Journal of The Electrochemical Society 160 (2013) A553. URL: https://iopscience.iop.org/article/10.1149/2.026304jes/meta. doi:10.1149/2.026304jes.
- [12] A. S. Bandarenka, K. Eckhard, A. Maljusch, W. Schuhmann, Localized Electrochemical Impedance Spectroscopy: Visualization of Spatial Distributions of the Key Parameters Describing Solid/Liquid Interfaces, Analytical Chemistry 85 (2013) 2443–2448. URL: https://doi.org/10.1021/ac303490t. doi:10.1021/ac303490t, publisher: American Chemical Society.
- [13] K. Eckhard, W. Schuhmann, Alternating cur-438 rent techniques in scanning electrochemical microscopy 439 1486-1497. (AC-SECM). Analyst 133 (2008)URL: 440 https://pubs.rsc.org/en/content/articlelanding/2008/an/b806721j. 441 doi:10.1039/B806721J, publisher: Royal Society of Chemistry. 442
- [14] K. Romanenko, P. W. Kuchel, A. Jerschow, Accurate Vi-443 sualization of Operating Commercial Batteries Using Spe-444 cialized Magnetic Resonance Imaging with Magnetic Field 445 32 (2020)Sensing, Chemistry of Materials 2107 - 2113.446 https://doi.org/10.1021/acs.chemmater.9b05246. URL: 447

- doi:10.1021/acs.chemmater.9b05246, publisher: American Chemical Society.
- mosing current distributions in batteries with magnetic resonance imaging, Journal of Magnetic Resonance 309 (2019) 106601. URL:
  http://www.sciencedirect.com/science/article/pii/S109078071930240X.
  doi:10.1016/j.jmr.2019.106601.
- metic resonance imaging of electrochemical cells: A perspective, Journal of Magnetic Resonance 308 (2019) 106600. URL: http://www.sciencedirect.com/science/article/pii/S1090780719302393. doi:10.1016/j.jmr.2019.106600.
- [17] A. J. Ilott, M. Mohammadi, C. M. Schauerman, M. J. Gan-460 Jerschow, Rechargeable lithium-ion cell state 461 magnetic charge and defect detection by in-situ inside-out 462 resonance imaging, Nature Communications 9 (2018) 1–7. 463 https://www.nature.com/articles/s41467-018-04192-x. URL: 464 doi:10.1038/s41467-018-04192-x. 465
- [18] K. Romanenko, A. Jerschow, Distortion-free inside-out imag-466 ing for rapid diagnostics of rechargeable Li-ion cells, Proceed-467 ings of the National Academy of Sciences 116 (2019) 18783-468 18789. URL: https://www.pnas.org/content/116/38/18783. 469 doi:10.1073/pnas.1906976116, publisher: National Academy of Sciences 470 Section: Physical Sciences. 471
- 472 [19] N. W. Halpern-Manners, V. S. Bajaj, T. Z. Teisseyre, A. Pines,
  473 Magnetic resonance imaging of oscillating electrical currents,
  474 Proceedings of the National Academy of Sciences 107 (2010)
  475 8519-8524. URL: https://www.pnas.org/content/107/19/8519.
  476 doi:10.1073/pnas.1003146107.
- Imaging periodic currents using alternating balanced steady-state free precession, Magnetic Resonance in Medicine 59 (2008) 140–148. URL:

  https://onlinelibrary.wiley.com/doi/abs/10.1002/mrm.21457.

  doi:10.1002/mrm.21457, \_eprint: https://onlinelibrary.wiley.com/doi/pdf/10.1002/mrm.21457

- [21] U. F. Mikac, Demšar, Κ. Berays. I. Serša. Mag-482 alternating netic resonance imaging of electric currents, 483 (2001)Magnetic Resonance Imaging 19 845 - 856. URL: 484 http://www.sciencedirect.com/science/article/pii/S0730725X01003939. 485 doi:10.1016/S0730-725X(01)00393-9. 486
- [22] M. J. Hamamura, L. T. Muftuler, O. Birgul, O. Nalcioglu, Measurement of ion diffusion using magnetic resonance electrical impedance tomography, Physics in Medicine and Biology 51 (2006) 2753–2762.
   doi:10.1088/0031-9155/51/11/005, publisher: IOP Publishing.
- [23] H. H. Eroğlu, M. Sadighi, B. M. Eyüboğlu, Induced Current Magnetic Resonance Electrical Conductivity Imaging With Oscillating Gradients, IEEE Transactions on Medical Imaging 37 (2018) 1606–1617.
   doi:10.1109/TMI.2018.2795718, conference Name: IEEE Transactions on Medical Imaging.
- S.-H. Park, |24| K. H. Kim, H.-I. Heo, Detection of fast 496 cillating magnetic fields using dynamic multiple TR 497 ing and Fourier analysis, PLoS ONE13 (2018). URL: 498 https://www.ncbi.nlm.nih.gov/pmc/articles/PMC5761850/. 499 doi:10.1371/journal.pone.0189916. 500
- 501 [25] H. Yang, G. G. Cook, M. N. J. Paley, Mapping of peri502 odic waveforms using the ghost reconstructed alternating cur503 rent estimation (GRACE) magnetic resonance imaging tech504 nique, Magnetic Resonance in Medicine 50 (2003) 633-637. URL:
  505 https://onlinelibrary.wiley.com/doi/abs/10.1002/mrm.10573.
  506 doi:10.1002/mrm.10573, \_eprint: https://onlinelibrary.wiley.com/doi/pdf/10.1002/mrm.10573
- [26] U. Westerhoff, K. Kurbach, F. Lienesch, M. Kurrat, Analysis of
  Lithium-Ion Battery Models Based on Electrochemical Impedance
  Spectroscopy, Energy Technology 4 (2016) 1620–1630. URL:
  https://onlinelibrary.wiley.com/doi/abs/10.1002/ente.201600154.
  doi:10.1002/ente.201600154, \_eprint: https://onlinelibrary.wiley.com/doi/pdf/10.1002/ente.20
- Α. Nauerth, Η. RARE |27| J.Hennig, Friedburg, imag-512 method MRing: fast imaging for clinical Mag-513 netic Resonance in Medicine 3 (1986)823-833. URL: 514

- https://onlinelibrary.wiley.com/doi/abs/10.1002/mrm.1910030602.
- doi:10.1002/mrm.1910030602, \_eprint: https://onlinelibrary.wiley.com/doi/pdf/10.1002/mrm.